

# Tunable correlated Chern insulator and ferromagnetism in a moiré superlattice

<https://doi.org/10.1038/s41586-020-2049-7>

Received: 16 May 2019

Accepted: 11 December 2019

Published online: 4 March 2020

 Check for updates

Guorui Chen<sup>1,2</sup>, Aaron L. Sharpe<sup>3,4</sup>, Eli J. Fox<sup>4,5</sup>, Ya-Hui Zhang<sup>6</sup>, Shaoxin Wang<sup>2</sup>, Lili Jiang<sup>2</sup>, Bosai Lyu<sup>7,8</sup>, Hongyuan Li<sup>1,2</sup>, Kenji Watanabe<sup>9</sup>, Takashi Taniguchi<sup>9</sup>, Zhiwen Shi<sup>7,8</sup>, T. Senthil<sup>6</sup>, David Goldhaber-Gordon<sup>4,5,12</sup>, Yuanbo Zhang<sup>8,10,11,12</sup> & Feng Wang<sup>1,2,12,13</sup>

Studies of two-dimensional electron systems in a strong magnetic field revealed the quantum Hall effect<sup>1</sup>, a topological state of matter featuring a finite Chern number  $C$  and chiral edge states<sup>2,3</sup>. Haldane<sup>4</sup> later theorized that Chern insulators with integer quantum Hall effects could appear in lattice models with complex hopping parameters even at zero magnetic field. The ABC-trilayer graphene/hexagonal boron nitride (ABC-TLG/hBN) moiré superlattice provides an attractive platform with which to explore Chern insulators because it features nearly flat moiré minibands with a valley-dependent, electrically tunable Chern number<sup>5,6</sup>. Here we report the experimental observation of a correlated Chern insulator in an ABC-TLG/hBN moiré superlattice. We show that reversing the direction of the applied vertical electric field switches the moiré minibands of ABC-TLG/hBN between zero and finite Chern numbers, as revealed by large changes in magneto-transport behaviour. For topological hole minibands tuned to have a finite Chern number, we focus on quarter filling, corresponding to one hole per moiré unit cell. The Hall resistance is well quantized at  $h/2e^2$  (where  $h$  is Planck's constant and  $e$  is the charge on the electron), which implies  $C=2$ , for a magnetic field exceeding 0.4 tesla. The correlated Chern insulator is ferromagnetic, exhibiting substantial magnetic hysteresis and a large anomalous Hall signal at zero magnetic field. Our discovery of a  $C=2$  Chern insulator at zero magnetic field should open up opportunities for discovering correlated topological states, possibly with topological excitations<sup>7</sup>, in nearly flat and topologically nontrivial moiré minibands.

Moiré superlattices in van der Waals heterostructures have emerged as a powerful tool for engineering quantum phenomena, because the periodic moiré potential defines new length and energy scales<sup>8–10</sup>. Notably, nearly flat electronic bands can be realized in different moiré superlattice systems, which offer exciting opportunities to realize a wide variety of correlation physics<sup>5,6</sup>. For example, correlated insulators and superconductivity have been reported in magic-angle twisted bilayer graphene<sup>11–13</sup> and in ABC-TLG/hBN moiré superlattices<sup>14,15</sup>, and spontaneous ferromagnetism and an anomalous Hall effect, apparently corresponding to an incipient Chern insulator, have been observed in twisted bilayer graphene with an aligned hBN layer<sup>16</sup>. Recent theories suggest that correlated topological phenomena could emerge in such graphene moiré superlattices, where a non-trivial band topology coexists with the nearly flat moiré miniband<sup>5,6,17,18</sup>. Pristine ABC-TLG, because of its cubic band and therefore a rather flat dispersion at low energy, can already exhibit strong correlations<sup>19</sup> and can potentially

host spontaneous quantum Hall states<sup>20</sup>. The moiré superlattice in ABC-TLG/hBN heterostructure further creates isolated flat moiré minibands, which enhances the electron–electron correlation and topological effects in the system. This ABC-TLG/hBN heterostructure provides a particularly attractive platform with which to explore correlated topological phenomena because not only the electron density but also the bandwidth and topology of the moiré minibands can be conveniently controlled by electrostatic gating<sup>5,6,14</sup>.

Here we report experimental observation of a correlated Chern insulator and ferromagnetism in ABC-TLG/hBN. Upon tuning the vertical displacement field, we show that the magneto-transport in an ABC-TLG/hBN moiré superlattice exhibits distinct behaviours for trivial minibands ( $C=0$ ) compared to topological minibands ( $C\neq 0$ ). A correlated Chern insulator with  $C=2$  quantum anomalous Hall effect<sup>21</sup> emerges around 1/4 filling of the topological hole miniband when the bandwidth is sufficiently narrowed by applying a displacement field

<sup>1</sup>Materials Science Division, Lawrence Berkeley National Laboratory, Berkeley, CA, USA. <sup>2</sup>Department of Physics, University of California at Berkeley, Berkeley, CA, USA. <sup>3</sup>Department of Applied Physics, Stanford University, Stanford, CA, USA. <sup>4</sup>Stanford Institute for Materials and Energy Sciences, SLAC National Accelerator Laboratory, Menlo Park, CA, USA. <sup>5</sup>Department of Physics, Stanford University, Stanford, CA, USA. <sup>6</sup>Department of Physics, Massachusetts Institute of Technology, Cambridge, MA, USA. <sup>7</sup>Key Laboratory of Artificial Structures and Quantum Control (Ministry of Education), School of Physics and Astronomy, Shanghai Jiao Tong University, Shanghai, China. <sup>8</sup>Collaborative Innovation Center of Advanced Microstructures, Nanjing, China. <sup>9</sup>National Institute for Materials Science, Tsukuba, Japan. <sup>10</sup>State Key Laboratory of Surface Physics and Department of Physics, Fudan University, Shanghai, China. <sup>11</sup>Institute for Nanoelectronic Devices and Quantum Computing, Fudan University, Shanghai, China. <sup>12</sup>Kavli Energy NanoSciences Institute at the University of California, Berkeley, and the Lawrence Berkeley National Laboratory, Berkeley, CA, USA. <sup>13</sup>e-mail: goldhaber-gordon@stanford.edu; zhyb@fudan.edu.cn; fengwang76@berkeley.edu

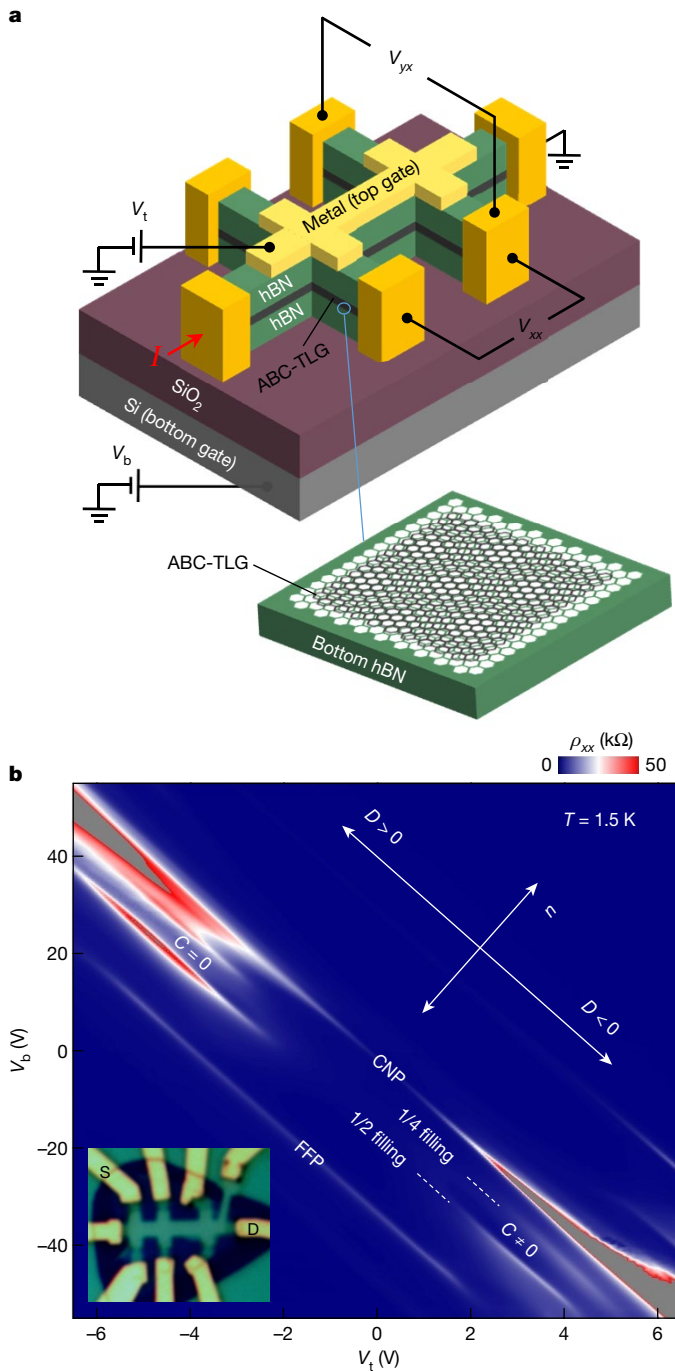


**Fig. 1 | ABC-TLG/hBN moiré superlattice and tunable Chern bands.** **a**, Schematic of the dual-gated ABC-TLG/hBN moiré superlattice Hall bar device and measurement configuration. The inset shows that the moiré pattern exists between ABC-TLG and bottom hBN. **b**, Colour plot of the longitudinal resistivity  $\rho_{xx}$  as a function of  $V_t$  and  $V_b$  at  $T = 1.5\text{ K}$ . The arrows show the direction of changing doping  $n$  and displacement field  $D$ , respectively. In addition to the band insulating states (characterized by the resistance peaks) at the charge neutral point (CNP) and fully filled point (FFP), tunable correlated insulator states also emerge at 1/4 filling and 1/2 filling of the hole minibands at large displacement field  $|D|$ . It has been predicted theoretically<sup>5,6</sup> that the hole miniband is topological (that is, Chern number  $C \neq 0$ ) for  $D < 0$  and trivial ( $C = 0$ ) for  $D > 0$ . The inset shows the optical image of the device.

in one direction. The correlated Chern insulator spontaneously breaks time-reversal symmetry, exhibiting strong ferromagnetic hysteresis and a zero-field anomalous Hall resistance over  $8\text{ k}\Omega$ . The experimentally observed  $C = 2$  Chern band can be understood theoretically by

incorporating electron–electron interaction effects on the quasi-particle band structure of ABC-TLG/hBN moiré minibands.

We fabricated two ABC-TLG/hBN moiré superlattice devices following the method described in ref.<sup>14</sup>. In brief, the ABC-TLG domain is identified by scanning near-field infrared nanoscopy<sup>22</sup> (Extended Data Fig. 1), and is isolated from adjacent ABA domains by atomic force microscope cutting<sup>23</sup>. The isolated ABC-TLG is then encapsulated in exfoliated hBN crystals, where one hBN crystal is aligned with the ABC-TLG to form the moiré superlattice. The ABC-TLG/hBN heterostructures are fabricated into a Hall bar geometry with one-dimensional edge contacts, a metal top gate, and a degenerately doped silicon bottom gate following standard nanofabrication procedures<sup>24</sup>. A schematic image and an optical image of device I (data shown in the main text is from device I) are shown in the insets to Fig. 1a, b (and Extended Data Fig. 2). Gate voltages  $V_t$  and  $V_b$  are applied to the metal top gate and the Si bottom gate, respectively. The dual-gate configuration allows us to independently control the doping and the miniband bandwidth of the ABC-TLG/hBN heterostructure<sup>25–27</sup>: the doping relative to the charge neutrality point is set by  $n = (D_b - D_t)/e$ , and the miniband bandwidth is tuned by the applied vertical displacement field  $D = (D_b + D_t)/2$ . Here  $D_b = +\varepsilon_b(V_b - V_b^0)/d_b$  and  $D_t = -\varepsilon_t(V_t - V_t^0)/d_t$  are the vertical displacement fields below and above the ABC-TLG/hBN moiré superlattice, respectively,  $\varepsilon_{b(t)}$  and  $d_{b(t)}$  are the dielectric constant and thickness of the bottom (top) dielectric layers, and  $V_{b(t)}^0$  is the effective offset in the bottom (top) gate voltages caused by environment-induced carrier doping. The longitudinal resistivity  $\rho_{xx}$  is obtained by  $\rho_{xx} = (W/L)V_{xx}/I$ , where  $W = 1\mu\text{m}$  is the channel width and  $L = 4\mu\text{m}$  is the channel length, and the Hall resistivity  $\rho_{yx}$  is obtained by  $\rho_{yx} = V_{yx}/I$  (the measurement configuration for the longitudinal and Hall voltages,  $V_{xx}$  and  $V_{yx}$ , respectively, is shown in Fig. 1a).

As the voltages applied to the gates are tuned, measurements of  $\rho_{xx}$  reveal several resistance peaks (Fig. 1b) in the ABC-TLG/hBN device across the parameter space controlled by  $V_t$  and  $V_b$ . In addition to the peaks corresponding to band insulating states at the charge neutrality point and fully filled point, tunable correlated insulator states emerge at 1/4 filling and 1/2 filling of the hole miniband (that is, one and two holes per moiré unit cell) when a finite displacement field  $|D|$  narrows the moiré minibands. There are two apparent asymmetries of the correlated insulator states in ABC-TLG/hBN at 1/4 and 1/2 charge fillings: between the electron and hole minibands, and between positive and negative  $D$ . Prominent correlated insulator states are observed in the hole minibands but not in the electron minibands because the hole miniband has a much smaller bandwidth for finite  $|D|$  (ref.<sup>14</sup>). The asymmetry between the positive and negative  $D$  fields arises from the fact that the moiré superlattice exists only between the ABC-TLG and the bottom hBN in this device (Fig. 1a). Interestingly, the direction of the displacement field has been predicted to determine not only the relative bandwidth but also the topology of the hole miniband. For a device with moiré superlattice between ABC-TLG and the bottom (top) hBN, a positive (negative)  $D$  leads to a trivial hole miniband with  $C = 0$  and smaller bandwidth, while a negative (positive)  $D$  leads to a topological hole miniband with  $C \neq 0$  and larger bandwidth<sup>5,6</sup>. The difference in bandwidth and topology is reflected in the electrical transport behaviour: in the device with the moiré superlattice at the bottom hBN, we observe stronger correlated insulators in the trivial hole miniband with positive  $D$ , because holes are easier to localize in the narrower trivial band than in the broader topological band with negative  $D$  (ref.<sup>17</sup>). Our previous studies have shown that superconductivity can emerge when we dope the 1/4 filling correlated insulator state in selected parameter spaces of the trivial hole miniband<sup>15</sup>.

To better probe the topological aspects of the moiré minibands, we turn to magneto-transport studies. At  $D = 0$ , the correlation effect in the system is relatively weak, and the magneto-transport data exhibit well defined quantum Hall states and a Landau fan diagram at low magnetic fields (see Extended Data Fig. 4), demonstrating the very

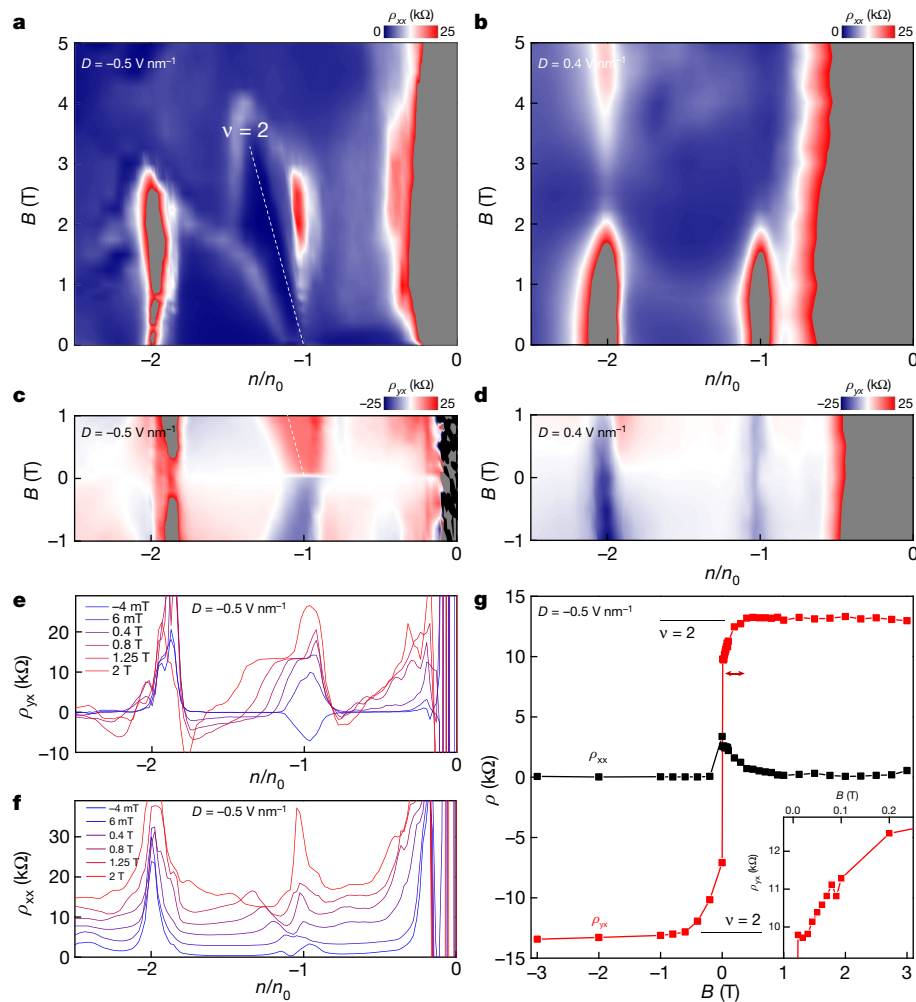


**Fig. 2 | Quantum Hall effect from the correlated  $C=2$  Chern insulator.**

**a, c,** Colour plot of  $\rho_{xx}$  (**a**) and  $\rho_{yx}$  (**c**) as a function of carrier density and magnetic field for the topological hole miniband at  $D = -0.5 \text{ V nm}^{-1}$  and  $T = 0.06 \text{ K}$ . The experimental data at  $T = 1.5 \text{ K}$  are qualitatively similar. **b, d,** Corresponding  $\rho_{xx}$  (**b**) and  $\rho_{yx}$  (**d**) plots for the trivial hole miniband at  $D = 0.4 \text{ V nm}^{-1}$  and  $T = 1.5 \text{ K}$ .  $n_0$  corresponds to the carrier density of the 1/4 filling of the first miniband. No quantum Hall signatures are present in the trivial hole miniband, whereas a  $v = 2$  quantum Hall effect characterized by a minimum of

$\rho_{xx}$  and a quantized  $\rho_{yx}$  emerges from 1/4 filling of the topological hole miniband. **e, f,** Horizontal line cuts of **a** and **c**, respectively. **e** shows that  $\rho_{yx}$  is well quantized beyond  $B = 0.4 \text{ T}$ . An offset of  $2.5 \text{ k}\Omega$  is applied for each stack in **f**. **g,** Line cut of  $\rho_{xx}$  and  $\rho_{yx}$  along the quantum Hall state (denoted by the dashed lines in **a** and **e**) shows that  $\rho_{yx}$  reaches a quantized value of  $v = 2$  at  $0.4 \text{ T}$ , and a large  $\rho_{yx}$  persists down to zero field. It represents a quantum anomalous Hall state for the  $C = 2$  correlated Chern insulator at 1/4 filling. The inset shows a zoomed-in plot of  $\rho_{yx}$  at small magnetic field.

high quality of our sample. With large displacement field, the moiré miniband bandwidth becomes narrower, and the dominant electron-electron interaction dramatically changes the magneto-transport behaviour. Figure 2a, b displays the colour plot of  $\rho_{xx}$  as a function of the hole doping and the vertical magnetic field  $B$  for  $D = -0.5 \text{ V nm}^{-1}$  (at  $T = 0.06 \text{ K}$ ) and  $D = 0.4 \text{ V nm}^{-1}$  (at  $T = 1.5 \text{ K}$ ), respectively. Figure 2c, d shows the corresponding Hall resistivity  $\rho_{yx}$  data. Experimental data for  $D = -0.5 \text{ V nm}^{-1}$  at  $1.5 \text{ K}$  exhibit qualitatively similar behaviour to those at  $0.06 \text{ K}$  (see Extended Data Fig. 3). We have used  $n_0 = 5.25 \times 10^{11} \text{ cm}^{-2}$  as the unit of carrier density, which corresponds to one hole per moiré lattice site (that is, 1/4 filling). The magneto-transport data exhibit distinct behaviours for the topological moiré miniband at negative  $D$  and the trivial miniband at positive  $D$  (refs. <sup>5,6</sup>). Specifically, a strong quantum Hall state emerges from the 1/4 filling point for  $D = -0.5 \text{ V nm}^{-1}$  but not for  $D = 0.4 \text{ V nm}^{-1}$ . The dashed line in Fig. 2a traces the minimum in  $\rho_{xx}$  following the relation  $n = veB/h$  for  $v = 2$ . This quantum Hall state is well developed at very low magnetic fields, and originates from the 1/4 filling resistive state at zero magnetic field (Fig. 2a). At the same time,  $\rho_{yx}$  is very large at weak magnetic fields and exhibits a jump in value when the magnetic field switches sign across  $B = 0 \text{ T}$  (Fig. 2c). By contrast,

stronger correlated insulator states are observed for  $D = 0.4 \text{ V nm}^{-1}$ , but no signatures of quantum oscillations or quantum Hall effects are present (Fig. 2b). In addition, Fig. 2d shows that the Hall resistivity signal tends to be rather small for all hole doping at  $D = 0.4 \text{ V nm}^{-1}$ . (The relatively large  $\rho_{yx}$  signals at 1/4 and 1/2 fillings are artefacts caused by crosstalk from the large  $\rho_{xx}$  of the correlated insulator states, and they do not change sign when the magnetic field is reversed.)

Figure 2e, f shows  $\rho_{yx}$  and  $\rho_{xx}$  as a function of density for a few representative magnetic field values, corresponding to horizontal line cuts in Fig. 2c and a, respectively.  $\rho_{yx}$  is well quantized for magnetic field larger than  $0.4 \text{ T}$  at the value of  $13.0 \pm 0.2 \text{ k}\Omega$ , that is, the expected quantized value of  $h/2e^2 = 12.9 \text{ k}\Omega$  is within the empirical uncertainty.  $\rho_{xx}$  exhibits a corresponding minimum in the quantum Hall state, with a minimum resistivity less than  $60 \Omega$  at  $2 \text{ T}$ . Figure 2g further displays  $\rho_{yx}$  and  $\rho_{xx}$  as a function of the magnetic field along the quantum Hall state following the dashed line in Fig. 2c, with the inset showing a zoomed-in plot of  $\rho_{yx}$  between 0 to 0.2 T.  $\rho_{yx}$  smoothly reaches the quantized value at  $0.4 \text{ T}$ .  $\rho_{yx}$  maintains a large though not quantized value all the way to zero magnetic field, and a large jump of  $\rho_{yx}$  is observed when the magnetic field changes sign.

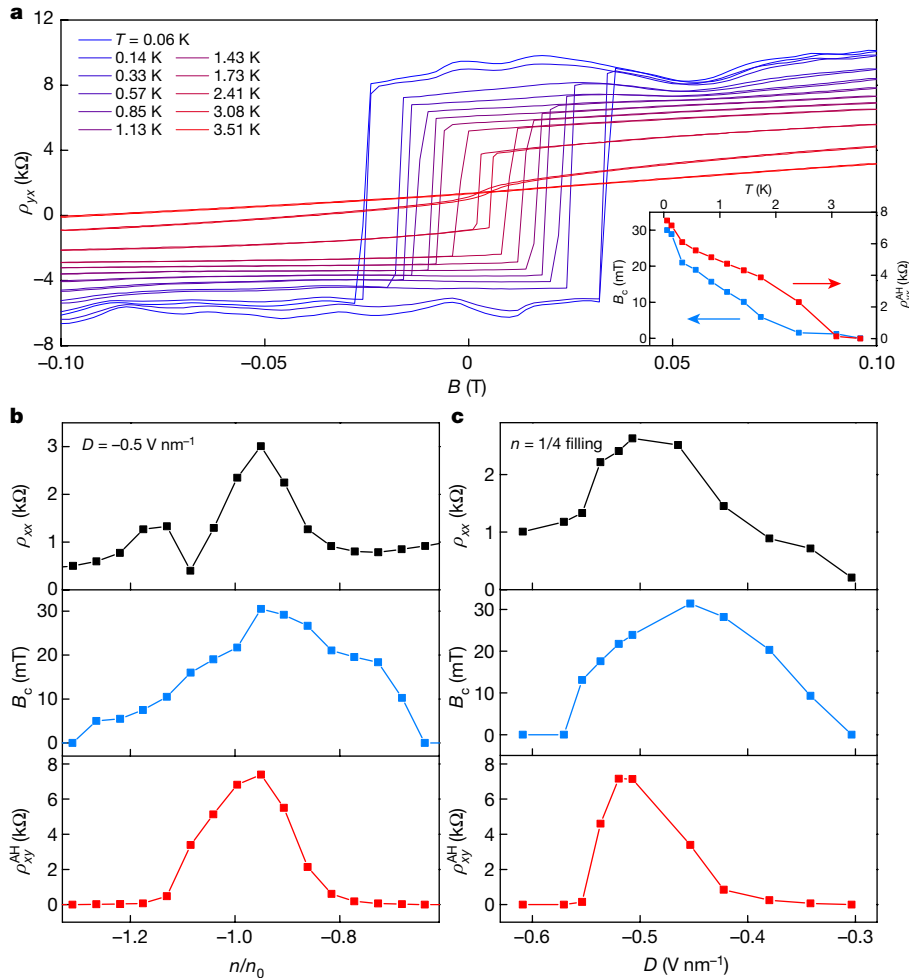


**Fig. 3 | Anomalous Hall effect and ferromagnetism.** **a**, Magnetic-field-dependent  $\rho_{yx}$  at 1/4 filling and  $D = -0.5 \text{ V nm}^{-1}$  at different temperatures. The Hall resistivity displays a clear anomalous Hall signal with strong ferromagnetic hysteresis. At the base temperature of  $T = 0.06 \text{ K}$ , the anomalous Hall signal can be as high as  $\rho_{yx}^{\text{AH}} = 8 \text{ k}\Omega$  and the coercive field is  $B_c = 30 \text{ mT}$ . The inset shows the extracted coercive field  $B_c$  and anomalous Hall signal  $\rho_{yx}^{\text{AH}}$  as a

function of temperature. **b**, The evolution of  $\rho_{xx}$ ,  $B_c$  and  $\rho_{yx}^{\text{AH}}$  as a function of hole doping at  $D = -0.5 \text{ V nm}^{-1}$ ,  $T = 0.06 \text{ K}$ . The strongest anomalous Hall signal is observed close to  $n = n_0$ . **c**, The evolution of  $\rho_{xx}$ ,  $B_c$  and  $\rho_{yx}^{\text{AH}}$  as a function of the displacement field  $D$  at  $n = n_0$ ,  $T = 0.06 \text{ K}$ . The strongest anomalous Hall signal is observed when the device is most insulating (that is, largest  $\rho_{xx}$ ).

The  $v=2$  quantum Hall state at 1/4 filling at  $D = -0.5 \text{ V nm}^{-1}$  cannot be explained by a conventional integer quantum Hall effect from single-particle Landau levels. Instead, we argue that it represents a quantum anomalous Hall state from a correlated Chern insulator. First, this quantum Hall state only exists at negative  $D$ , where the miniband is predicted to have a non-trivial Chern number, and is absent at the positive  $D$ , where the band is predicted to be trivial. Second, it is well established that the lowest single-particle Landau level in ABC-TLG should be a  $v=3$  state owing to a winding number of 3 close to the valence band maximum<sup>28</sup>. Third, only one quantum Hall state is observed anywhere, and the quantized Hall resistivity appears to start at very low magnetic field. If the observed quantum Hall state of 1/4 filling at  $D = -0.5 \text{ V nm}^{-1}$  is from the lowest single-particle Landau level, similar Landau levels should also exist close to the charge neutrality point and the 1/2 filling correlated insulators, and higher Landau levels should be observable. (See Extended Data Fig. 4 for a single-particle Landau fan diagram in the same device, where  $D = 0$  and the electron correlation is weak.) Finally, an apparent non-zero quantum Hall-like gap was observed for the 1/4 filling Chern insulator state down to  $B = 0 \text{ T}$ ; the size of the gap continuously increases with increasing  $B$  (see Methods and Extended Data Fig. 5). All our data can be naturally explained by a  $v=2$  Chern insulator state at 1/4 filling. Such a  $C=2$  correlated Chern insulator should feature quantized Hall resistivity  $\rho_{yx}$  and a corresponding magnetic

field dependent carrier density based on the Streda formula<sup>29</sup>. This Chern insulator at 1/4 filling is a strongly correlated state that breaks the valley degeneracy and fills only the  $C=2$  electronic band in one valley. The nearly flat and tunable moiré minibands in the ABC-TLG/hBN moiré heterostructure are critical for the realization of such a correlated topological state.

The correlated Chern insulator, persisting to zero magnetic field, spontaneously breaks the time-reversal symmetry and can generate valley-flavour ferromagnetism at 1/4 filling. Indeed, ferromagnetism and strong anomalous Hall signals emerge from the Chern insulator state at zero magnetic field. Figure 3a shows the temperature-dependent Hall resistivity when a small perpendicular  $B$  is swept between  $-0.1 \text{ T}$  and  $0.1 \text{ T}$ . The Hall resistivity displays a clear anomalous Hall signal with strong ferromagnetic hysteresis. At  $B = 0 \text{ T}$ ,  $\rho_{yx}$  is non-zero and depends on the magnetic field sweep direction, a defining ferromagnetic feature. At the base temperature of  $T = 0.06 \text{ K}$ , the anomalous Hall signal reaches a maximum of  $\rho_{yx}^{\text{AH}} = 8 \text{ k}\Omega$  and a coercive field as large as  $B_c = 30 \text{ mT}$ . The inset in Fig. 3a shows the temperature dependence of  $\rho_{yx}^{\text{AH}}$  and  $B_c$ : both signals decrease monotonically with increasing temperature, reaching zero at  $T = 3.5 \text{ K}$ . The zero magnetic field  $\rho_{yx}^{\text{AH}}$  is already close to  $12.9 \text{ k}\Omega$ . An almost perfect quantization of the  $C=2$  quantum anomalous Hall<sup>18</sup> Chern insulator appears at a magnetic field as low as  $0.4 \text{ T}$ .

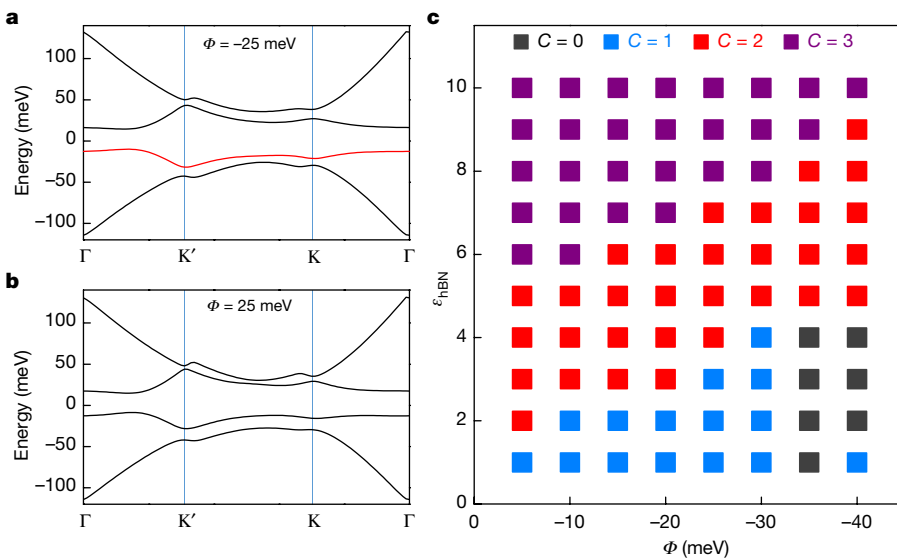


**Fig. 4 | Calculated Chern number including the electron–electron interaction effects.** **a, b,** Calculated single-particle band structure of the ABC-TLG/hBN moiré superlattice for  $\Phi = -25 \text{ meV}$  and  $25 \text{ meV}$ , respectively. Here  $\Phi$  is the energy difference between the top and bottom layers of ABC-TLG, and  $\Phi = -25 \text{ meV}$  corresponds to the vertical displacement field around  $D = -0.5 \text{ V nm}^{-1}$ . The red line highlights the topological hole miniband for

$\Phi = -25 \text{ meV}$ . **c,** Calculated Chern number of the hole miniband as a function of the energy difference  $\Phi$  and the effective dielectric constant  $\epsilon_{\text{hBN}}$  after including the electron–electron interaction effects using the Hartree–Fock approximation. The resulting band Chern number can be 2 for parameters close to the experimental device where  $\Phi \approx -25 \text{ meV}$  and  $\epsilon_{\text{hBN}} \approx 4$ .

The ferromagnetism is tunable by  $n$  and  $D$  and appears only in a limited parameter space of  $n$  and  $D$ . In Fig. 2e,  $\rho_{yx}$  near  $n = n_0$  presents different signs at  $B = -4 \text{ mT}$  and  $6 \text{ mT}$ , which is much smaller than  $B_c$ . For this measurement, the magnetic field is fixed and carrier density is swept from a non-ferromagnetic state to a ferromagnetic state, which leads to  $\rho_{yx}$  with different signs even in small positive and negative magnetic fields. A clearer  $n$ -dependence of  $\rho_{xx}$ ,  $B_c$  and  $\rho_{yx}^{\text{AH}}$  at  $D = -0.5 \text{ V nm}^{-1}$  at the base temperature is shown in Fig. 3b by sweeping the magnetic field at different fixed  $n$ .  $B_c$  and  $\rho_{yx}^{\text{AH}}$  both have maximum values close to  $n = n_0$ . However,  $\rho_{yx}^{\text{AH}}$  shows a stronger carrier doping dependence and decreases to almost zero at  $n = n_0 \pm 0.2n_0$ , while  $B_c$  decreases to zero at  $n = n_0 \pm 0.35n_0$ .  $\rho_{xx}$  displays an unusual behaviour with both a resistance peak and a resistance dip close to  $n = n_0$ , the origin of which requires further experimental and theoretical study. Figure 3c shows the  $D$ -dependence of  $\rho_{xx}$ ,  $B_c$  and  $\rho_{yx}^{\text{AH}}$  at  $n = n_0$ .  $\rho_{xx}$  shows a maximum at  $D = -0.5 \text{ V nm}^{-1}$ , which might be due to the narrowest bandwidth and strongest correlation effects at this displacement field<sup>14</sup>.  $\rho_{yx}^{\text{AH}}$  also shows a maximum at  $D = -0.5 \text{ V nm}^{-1}$ , suggesting the importance of electron–electron correlations to the observed anomalous Hall signal. A finite  $\rho_{yx}^{\text{AH}}$  can be observed with  $D$  between  $-0.3 \text{ V nm}^{-1}$  and  $-0.57 \text{ V nm}^{-1}$ . A non-zero  $B_c$  is present in the same  $D$  range, although the maximum  $B_c$  appears at  $D = -0.45 \text{ V nm}^{-1}$ .

The observed  $C = 2$  correlated Chern insulator can be understood theoretically from the topological moiré minibands when the electron–electron interactions are considered. Previous theoretical calculations predict a valley Chern number  $C = 3$  for the single-particle hole miniband for negative  $D$  (refs. <sup>5,6</sup>), but our results suggest that interaction effects can renormalize the valley Chern number. Figure 4a, b shows the single-particle band structures of the lowest few moiré minibands in ABC-TLG/hBN moiré superlattices for positive and negative displacement fields. For the negative  $D$  values (supporting a non-zero valley Chern number), the valence band overlaps with the remote lower band (see Fig. 4a). We incorporate the interaction effects in Hartree–Fock theory. When the valence band is close to the band below (at large  $|D|$ ) or when the interaction strength is sufficiently strong (with small dielectric constant), the self-energy corrections mix the valence band and the lower band, leading to reduction of the Chern number to  $C = 2$ . As shown in Fig. 4c, when the dielectric constant is around 4 (effective screening from the

dielectric constant of hBN), the valley Chern number is expected to be 2 for a large range of displacement field values.

Our observation of a tunable  $C = 2$  Chern insulator in ABC-TLG/hBN moiré superlattice provides an opportunity to explore correlated topological states in van der Waals moiré heterostructures. For example, fractional Chern insulators and non-Abelian states could emerge from strong correlations in nearly flat topological minibands once the quality of moiré heterostructures is further improved. In particular, the flat  $C = 2$  Chern band has the potential to host novel fractional Chern insulator states beyond the fractional quantum Hall paradigm<sup>30,31</sup>.

## Online content

Any methods, additional references, Nature Research reporting summaries, source data, extended data, supplementary information, acknowledgements, peer review information; details of author contributions and competing interests; and statements of data and code availability are available at <https://doi.org/10.1038/s41586-020-2049-7>.

1. Klitzing, K. v., Dorda, G. & Pepper, M. New method for high-accuracy determination of the fine-structure constant based on quantized Hall resistance. *Phys. Rev. Lett.* **45**, 494–497 (1980).
2. Thouless, D. J., Kohmoto, M., Nightingale, M. P. & den Nijs, M. Quantized Hall conductance in a two-dimensional periodic potential. *Phys. Rev. Lett.* **49**, 405–408 (1982).
3. Xiao, D., Chang, M.-C. & Niu, Q. Berry phase effects on electronic properties. *Rev. Mod. Phys.* **82**, 1959–2007 (2010).
4. Haldane, F. D. M. Model for a quantum Hall effect without Landau levels: condensed-matter realization of the ‘parity anomaly’. *Phys. Rev. Lett.* **61**, 2015–2018 (1988).
5. Chittari, B. L., Chen, G., Zhang, Y., Wang, F. & Jung, J. Gate-tunable topological flat bands in trilayer graphene boron-nitride moiré superlattices. *Phys. Rev. Lett.* **122**, 016401 (2019).
6. Zhang, Y.-H., Mao, D., Cao, Y., Jarillo-Herrero, P. & Senthil, T. Nearly flat Chern bands in moiré superlattices. *Phys. Rev. B* **99**, 075127 (2019).
7. Bergholtz, E. J. & Liu, Z. Topological flat band models and fractional Chern insulators. *Int. J. Mod. Phys. B* **27**, 1330017 (2013).
8. Dean, C. R. et al. Hofstadter’s butterfly and the fractal quantum Hall effect in moiré superlattices. *Nature* **497**, 598–602 (2013).
9. Ponomarenko, L. A. et al. Cloning of Dirac fermions in graphene superlattices. *Nature* **497**, 594–597 (2013).
10. Hunt, B. et al. Massive Dirac fermions and Hofstadter butterfly in a van der Waals heterostructure. *Science* **340**, 1427–1430 (2013).
11. Cao, Y. et al. Correlated insulator behaviour at half-filling in magic-angle graphene superlattices. *Nature* **556**, 80–84 (2018).

12. Cao, Y. et al. Unconventional superconductivity in magic-angle graphene superlattices. *Nature* **556**, 43–50 (2018).
13. Lu, X. et al. Superconductors, orbital magnets, and correlated states in magic angle bilayer graphene. *Nature* **574**, 653–657 (2019).
14. Chen, G. et al. Evidence of a gate-tunable Mott insulator in a trilayer graphene moiré superlattice. *Nat. Phys.* **15**, 237 (2019).
15. Chen, G. et al. Signatures of tunable superconductivity in a trilayer graphene moiré superlattice. *Nature* **572**, 215–219 (2019).
16. Sharpe, A. L. et al. Emergent ferromagnetism near three-quarters filling in twisted bilayer graphene. *Science* **365**, 605–608 (2019).
17. Zhang, Y.-H. & Senthil, T. Bridging Hubbard model physics and quantum Hall physics in trilayer graphene hBN moiré superlattice. *Phys. Rev. B* **99**, 205150 (2019).
18. Liu, J., Ma, Z., Gao, J. & Dai, X. Quantum valley Hall effect, orbital magnetism, and anomalous hall effect in twisted multilayer graphene systems. *Phys. Rev. X* **9**, 031021 (2019).
19. Lee, Y. et al. Competition between spontaneous symmetry breaking and single-particle gaps in trilayer graphene. *Nat. Commun.* **5**, 5656 (2014).
20. Zhang, F., Jung, J., Fiete, G. A., Niu, Q. & MacDonald, A. H. Spontaneous quantum Hall states in chirally stacked few-layer graphene systems. *Phys. Rev. Lett.* **106**, 156801 (2011).
21. Chang, C.-Z. et al. Experimental observation of the quantum anomalous Hall effect in a magnetic topological insulator. *Science* **340**, 167–170 (2013).
22. Ju, L. et al. Topological valley transport at bilayer graphene domain walls. *Nature* **520**, 650–655 (2015).
23. Li, H. et al. Electrode-free anodic oxidation nanolithography of low-dimensional materials. *Nano Lett.* **18**, 8011–8015 (2018).
24. Wang, L. et al. One-dimensional electrical contact to a two-dimensional material. *Science* **342**, 614–617 (2013).
25. Zhang, Y. et al. Direct observation of a widely tunable bandgap in bilayer graphene. *Nature* **459**, 820–823 (2009).
26. Zou, K., Zhang, F., Clapp, C., MacDonald, A. H. & Zhu, J. Transport studies of dual-gated ABC and ABA trilayer graphene: band gap opening and band structure tuning in very large perpendicular electric fields. *Nano Lett.* **13**, 369–373 (2013).
27. Lui, C. H., Li, Z., Mak, K. F., Cappelluti, E. & Heinz, T. F. Observation of an electrically tunable band gap in trilayer graphene. *Nat. Phys.* **7**, 944–947 (2011).
28. Zhang, L., Zhang, Y., Camacho, J., Khodas, M. & Zaliznyak, I. The experimental observation of quantum Hall effect of  $l=3$  chiral quasiparticles in trilayer graphene. *Nat. Phys.* **7**, 953–957 (2011).
29. MacDonald, A. The Quantum Hall Effects. In *Quantum Coherence in Mesoscopic Systems* (ed. Kramer, B.) 195–217 (Springer, 1991).
30. Liu, Z., Bergholtz, E. J., Fan, H. & Läuchli, A. M. Fractional Chern insulators in topological flat bands with higher Chern number. *Phys. Rev. Lett.* **109**, 186805 (2012).
31. Wang, Y.-F., Yao, H., Gong, C.-D. & Sheng, D. N. Fractional quantum Hall effect in topological flat bands with Chern number two. *Phys. Rev. B* **86**, 201101 (2012).

**Publisher's note** Springer Nature remains neutral with regard to jurisdictional claims in published maps and institutional affiliations.

© The Author(s), under exclusive licence to Springer Nature Limited 2020

# Article

## Methods

### Transport measurements

The ultralow temperature measurement is performed in a dilution refrigerator. Low-temperature electronic filtering, including microwave filters, low-pass resistor-capacitor filters, and thermal meanders, is used to anchor the electron temperature as well as to prevent quasiparticle excitations from high-frequency noise. Stanford Research Systems SR830 lock-in amplifiers with NF Corporation LI-75A voltage preamplifiers are used to measure the resistivity of the device with an alternating-current bias current of 0.5 nA at a frequency of 7 Hz.

### The nature of the correlated insulator at 1/4 filling for the topological side

Because of the Wannier obstruction caused by the valley Chern number, a standard Mott insulator with localized charge is impossible<sup>17</sup>. Therefore, the physics on the topological side is essentially different from that on the trivial side, despite the similarity between the band structures. Because a narrow Chern band is analogous to a Landau level, the physics on the topological side is similar to that of quantum Hall systems with spin and valley degeneracies. At 1/4 filling, when the band is sufficiently flat, a single fully filled spin- and valley-polarized Chern band is favoured<sup>6</sup>, similar to the “quantum Hall ferromagnetism” found in Landau levels<sup>32</sup>. A valley-polarized Chern insulator matches the current transport experiment quite well. Ideally, a fully filled Chern band leads to quantized Hall conductivity  $\sigma_{yx} = 2e^2/h$ . At zero magnetic field, domains formed by the two degenerate valleys can cause a finite  $\rho_{xx}$  on the order of  $h/e^2$ . Upon increasing the magnetic field to about 0.4 T, the valley Zeeman coupling<sup>17</sup> can align the domains and lead to perfect quantization of the Hall conductivity.

Ferromagnetism and an anomalous Hall effect have also recently been observed in a near-magic-angle twisted bilayer graphene moiré superlattice at 3/4 filling of the conduction miniband, where an hBN cladding layer appears to be aligned with the proximate graphene<sup>16</sup>. These effects are likely to have a similar origin in both systems, where electron-electron interactions create a spontaneous valley polarization in the nearly flat and topological moiré minibands<sup>33,34</sup>. However, the Hall resistance in the incipient Chern insulator state of the twisted bilayer graphene device of ref. <sup>16</sup> is not quantized even under a finite applied magnetic field, possibly owing to substantial twist-angle disorder<sup>35</sup>.

### Calculation for ABC-TLG/hBN moiré superlattice

A simple argument in ref. <sup>6</sup> shows that the valley Chern number must jump by 3 when switching the direction of the displacement field if the super-lattice gap does not close during this process. A direct numerical calculation gives  $C=3$  for the  $D < 0$  side. Thus, owing to the interactions, a symmetry breaking state with spin-valley polarization is stabilized, and then a Chern insulator with  $C=3$  is expected. We first improve our theoretical modelling of the band structure by adding various remote-hopping terms at the single-particle level and incorporating interaction effects, as shown in Extended Data Fig. 6. As we will show,  $C=3$  is still robust in our more sophisticated model of single-particle band structure. Interaction effects turn out to be necessary to explain the reduction of the Chern number.

The ABC-TLG is modelled by a six-band model. We use the following parameters<sup>36</sup>:  $(v, \gamma_1, \gamma_2, \gamma_3, \gamma_4) = (2,676, 380, 8.3, 260, 104)$  meV.

Then the Hamiltonian for the valley + is:

$$H_0(\mathbf{k}) = \begin{pmatrix} V/2 & v(k_x - ik_y) & -v_4(k_x - ik_y) & v_3(k_x + ik_y) & 0 & \gamma_2 \\ v(k_x + ik_y) & V/2 & 0 & 0 & 0 & 0 \\ -v_4(k_x + ik_y) & \gamma_1 & v(k_x + ik_y) & v(k_x - ik_y) & -v_4(k_x - ik_y) & v_3(k_x + ik_y) \\ v_3(k_x - ik_y) & 0 & v(k_x + ik_y) & 0 & \gamma_1 & 0 \\ 0 & 0 & -v_4(k_x + ik_y) & \gamma_1 & -\gamma/2 & v(k_x - ik_y) \\ \gamma_2 & 0 & v_3(k_x - ik_y) & 0 & v(k_x + ik_y) & -\gamma/2 \end{pmatrix}$$

The aligned hBN layer in the bottom provides a moiré hopping term which folds the original band structure to a small mini Brillouin zone. We use the same model of the moiré hopping term as in ref. <sup>37</sup>.

Using the above model we get the band structures shown in Fig. 4. For  $\Phi_V = -25$  meV (where subscript V indicates ‘vertical’) we get a narrow valence band with Chern number  $|C|=3$ . We have tried to change the various hopping parameters and the potential difference. However, the Chern number is always equal to 3 and we conclude that  $C=2$  cannot be reproduced at the single-particle level.

In Fig. 4b, we can see that although at each K-point the valence band is isolated from the band below, they overlap in energy (in other words, although there is a direct gap there is no indirect gap). More precisely, the system is in a compensated semimetal phase at the fully filled point. This is in agreement with the experimental measurement. On the  $D < 0$  side, electrons are pushed away from the aligned bottom hBN layer. Therefore the moiré superlattice potential has a weaker effect and the superlattice gap is small.

Given that the valence band is not isolated from the remote band below, an interaction-induced self-energy can renormalize the band structure and maybe even the band topology. To incorporate this effect, we perform a self-consistent Hartree–Fock calculation by keeping only the valence band and the remote band. The interacting Hamiltonian is

$$H = \sum_{k;a,\sigma} \sum_m \xi_{a,m}(\mathbf{k}) c_{a,\sigma;m}^\dagger(\mathbf{k}) c_{a,\sigma;m}(\mathbf{k}) + \frac{1}{N} \sum_{\mathbf{q}} \sum_{\mathbf{k}_1, \mathbf{k}_2; a_1, \sigma_1, a_2, \sigma_2} c_{a_1, \sigma_1; m_1}^\dagger(\mathbf{k}_1 + \mathbf{q}) c_{a_2, \sigma_2; m_2}^\dagger(\mathbf{k}_2 - \mathbf{q}) c_{a_2, \sigma_2; n_2}(\mathbf{k}_2) c_{a_1, \sigma_1; n_1}(\mathbf{k}_1) V(\mathbf{q}) \lambda_{a_1; m_1, n_1}(\mathbf{k}_1, \mathbf{q}) \lambda_{a_2; m_2, n_2}(\mathbf{k}_2, -\mathbf{q})$$

where  $a = \pm$  is the valley index and  $m = 0, 1$  is the band index, labelling the valence band and the remote band.  $\sigma = \uparrow, \downarrow$  is the spin index.  $c_{a,a;m}(\mathbf{k})$  is the creation operator corresponding to the band  $m$  for the valley  $a$  and spin  $\sigma$ . The two terms in the Hamiltonian are the kinetic term and the interaction term.  $V(q)$  is the screened Coulomb interaction controlled by the renormalization factor of the dielectric constant. In the interaction we have included the form factors  $\lambda_{a,mn}$  to incorporate the Berry curvature of the Bloch wavefunctions<sup>6</sup>. Then Hartree–Fock self-energy can be obtained from the self-consistent equations:

$$\Sigma_{a,mn}^H(\mathbf{k}) = \frac{1}{N} \sum_{a_2, \sigma; m'} \sum_{\mathbf{G}} \sum_{\mathbf{k}_2} c_{a_2, \sigma; m'}^\dagger(\mathbf{k}_2) V(G) \lambda_{a; mn}(\mathbf{k}, \mathbf{G}) \lambda_{a_2; m'm'}(\mathbf{k}_2, -\mathbf{G})$$

$$\Sigma_{a,mn}^F(\mathbf{k}) = -\frac{1}{N} \sum_{m'} \sum_{\mathbf{q}} c_{a\sigma; m'}^\dagger(\mathbf{k} + \mathbf{q}) c_{a, \sigma; m}(\mathbf{k} + \mathbf{q}) V(\mathbf{q}) \lambda_{a; m'n}(\mathbf{k}, \mathbf{q}) \lambda_{a; mm'}(\mathbf{k} + \mathbf{q}, -\mathbf{q})$$

We solve these equations by iterating from zero initial values. Then we add the self-energies to calculate the new Chern number. The result is summarized in Fig. 4c. When the dielectric constant is large, the Chern number is 3, the same as the non-interacting case. For a fixed displacement field, increasing the interaction strength (decreasing the dielectric constant) can reduce the Chern number to 2 through a topological transition. For a large parameter region,  $C=2$  is indeed expected, consistent with the current experiment.

Finally, we discuss the nature of the observed Chern insulator. At 1/4 filling, there is one particle per moiré unit cell. Within Hartree–Fock theory<sup>6</sup>, the most natural ground state is a spin- and valley-polarized Chern insulator with  $C=2$ , which is consistent with the transport measurement.

Because the two valleys are degenerate at zero magnetic field, domains can exist and cause the non-quantization of the Hall conductivity owing to the chiral edge mode in the domain boundary. Upon increasing the magnetic field, the valley Zeeman coupling can align the domains and lead to perfect quantization. In the current experiment,

the quantization is achieved at only 0.2 T, which suggests that the valley Zeeman coupling is large, consistent with previous theoretical calculations<sup>17</sup>.

The anomalous Hall effect in Fig. 3 strongly suggests that the valley is polarized. Although the simplest ansatz within mean field theory also requires spin polarization, the present transport measurement cannot rule out more exotic Chern insulator phases with the spins in a disordered (for example, ‘spin liquid’) or anti-ferromagnetic phase. Even for a simple spin-polarized scenario, non-trivial topological defects in spin space may have an important role. The skyrmion excitation carries charge  $Q = 2e$  in the Chern insulator and may be the cheapest charge excitation (at small field the cheapest charge excitations may also be valley flips). In this case the activation gap is decided by the skyrmion gap. The existence of skyrmions may be reflected in a large g factor (skyrmions involve many spin flips) for response of activation gap to magnetic field. We leave it to future experiments to probe these possible interesting physics associated with the spin texture.

## Insulating behaviour and extracted gap of the Chern insulator state

We measured the magnetic-field-dependent energy gap of the  $v = 2$  state. Extended Data Fig. 5 shows the temperature dependent lon-

tudinal resistivity  $\rho_{xx}$  and conductivity  $\sigma_{xx} = \rho_{xx} / (\rho_{xx}^2 + \rho_{yx}^2)$ , at different magnetic field  $B$  for the  $v = 2$  state. For all magnetic fields, the temperature dependencies in Extended Data Fig. 5a, b exhibit typical behaviours of the quantum Hall insulator in that both  $\rho_{xx}$  and  $\sigma_{xx}$  decreases with decreasing temperature, which differs from a trivial insulator behaviour where the decrease in  $\sigma_{xx}$  is accompanied by a divergence in  $\rho_{xx}$ . This quantum-Hall-like behaviour persists at zero magnetic field. Extended Data Fig. 5c shows the energy gap at different magnetic fields, obtained by fitting the data to an Arrhenius activation model of  $\sigma_{xx} \propto e^{-4/2k_B T}$ . The deviation from the Arrhenius behaviour at the low- and high-temperature limits is possibly due to the variable range hopping at low temperatures and strong thermal excitations at high temperatures. We extract a non-zero energy gap of about 2 K at  $B = 0$ . We can clearly see a continuous increase in gap size with increasing the magnetic field from  $B = 0$ , and the non-zero intercept at  $B = 0$ . It indicates that quantum Hall behaviour extends to zero magnetic field, consistent with the Chern insulator state.

## Ferromagnetism and Chern insulator in a second device

Similar ferromagnetism and Chern insulator data have been observed in a second ABC-TLG/hBN device. Extended Data Fig. 7 shows the basic characterization of the second device (device II, Extended Data Fig. 7a). The moiré exists between the top hBN and ABC-TLG for device II (Extended Data Fig. 7b, opposite to that of device I in the main text). This leads to a non-trivial band at positive displacement fields and a trivial band at negative displacement fields. Extended Data Fig. 7c shows the Mott insulating states at 1/4 and 1/2 fillings of the trivial band for negative displacement fields, and weak resistance peaks of the non-trivial band for the positive displacement fields.

By tuning the gate voltages to the non-trivial side at the positive displacement field near 1/4 filling, we reproduced the main data of device I in the main text. Extended Data Fig. 8 shows the main results

for device II. At  $D = 0.55 \text{ V nm}^{-1}$ , an anomalous Hall hysteresis loop is clearly resolved. We show the  $n$ - and  $D$ -dependence of the anomalous Hall resistivity  $\rho_{yx}^{\text{AH}}$  and the coercive field  $B_c$  in Extended Data Fig. 8b. The fans of  $\rho_{xx}$  and  $\rho_{yx}$  in Extended Data Fig. 8c, d show the clear  $v = 2$  state developing from 1/4 filling, as represented by the dashed lines. (The contact resistances are much larger in device II, which leads to much larger measurement noise. It also prevents us from measuring the magneto-transport at the lowest dilution fridge temperatures owing to the increased contact resistances at low temperature.)

## Data availability

The data that support the findings of this study are available from the corresponding authors upon reasonable request.

32. Young, A. F. et al. Spin and valley quantum Hall ferromagnetism in graphene. *Nat. Phys.* **8**, 550–556 (2012).
33. Bultinck, N., Chatterjee, S. & Zaletel, M. P. Anomalous Hall ferromagnetism in twisted bilayer graphene. Preprint at <https://arxiv.org/abs/1901.08110> (2019).
34. Zhang, Y.-H., Mao, D. & Senthil, T. Twisted bilayer graphene aligned with hexagonal boron nitride: anomalous Hall effect and a lattice model. Preprint at <https://arxiv.org/abs/1901.08209> (2019).
35. Yoo, H. et al. Atomic and electronic reconstruction at the van der Waals interface in twisted bilayer graphene. *Nat. Mater.* **18**, 448–453 (2019).
36. Zhang, F., Sahu, B., Min, H. & MacDonald, A. H. Band structure of ABC-stacked graphene trilayers. *Phys. Rev. B* **82**, 035409 (2010).
37. Jung, J., Raoux, A., Qiao, Z. & MacDonald, A. H. Ab initio theory of moiré superlattice bands in layered two-dimensional materials. *Phys. Rev. B* **89**, 205414 (2014).

**Acknowledgements** We thank Y. Yu and M. Sui for measurement assistance, and acknowledge discussions with M. Zaletel, E. Altman, J. Jung and M. A. Kastner. G.C. and F.W. were supported as part of the Center for Novel Pathways to Quantum Coherence in Materials, an Energy Frontier Research Center funded by the US Department of Energy, Office of Science, Basic Energy Sciences. A.L.S. was supported by a National Science Foundation Graduate Research Fellowship and a Ford Foundation Predoctoral Fellowship. The work of E.J.F. and D.G.-G. on this project was supported by the US Department of Energy, Office of Science, Basic Energy Sciences, Materials Sciences and Engineering Division, under contract number DE-AC02-76SF00515. Low-temperature infrastructure (dilution fridges) and cryostat support were funded in part by the Gordon and Betty Moore Foundation through grant number GBMF3429. Part of the sample fabrication was conducted at the Nano-fabrication Laboratory at Fudan University. Part of the measurement was performed in Oxford Instrument Nanoscience Shanghai Demo Laboratory. Y.Z. acknowledges financial support from National Key Research Program of China (grant numbers 2016YFA0300703, 2018YFA0305600), NSF of China (grant numbers U1732274, 11527805, 11425415 and 11421404), and the Strategic Priority Research Program of Chinese Academy of Sciences (grant number XDB30000000). Z.S. acknowledges support from National Key Research and Development Program of China (grant number 2016YFA0302001) and National Natural Science Foundation of China (grant number 11574204, 11774224), and additional support from a Shanghai talent programme. T.S. was supported by NSF grant DMR-1608505, and partially through a Simons Investigator Award from the Simons Foundation. K.W. and T.T. acknowledge support from the Elemental Strategy Initiative conducted by the MEXT, Japan and the CREST (JPMJCR15F3), JST.

**Author contributions** F.W. and G.C. conceived the project. F.W., Y.Z., D.G.-G. and T.S. supervised the project. G.C. fabricated samples and performed transport characterizations at temperature above 1 K to first identify the  $C = 2$  quantum Hall states. G.C., A.L.S. and E.J.F. performed ultralow temperature transport measurements. G.C., L.J., B.L., H.L. and Z.S. prepared TLG and performed near-field infrared and atomic force microscope measurements. K.W. and T.T. grew hBN single crystals. Y.-H.Z. and T.S. calculated the band structures and Chern numbers. G.C., A.L.S., E.J.F., Y.-H.Z., T.S., D.G.-G., Y.Z. and F.W. analysed the data. G.C., Y.-H.Z., T.S. and F.W. wrote the paper, with input from all authors.

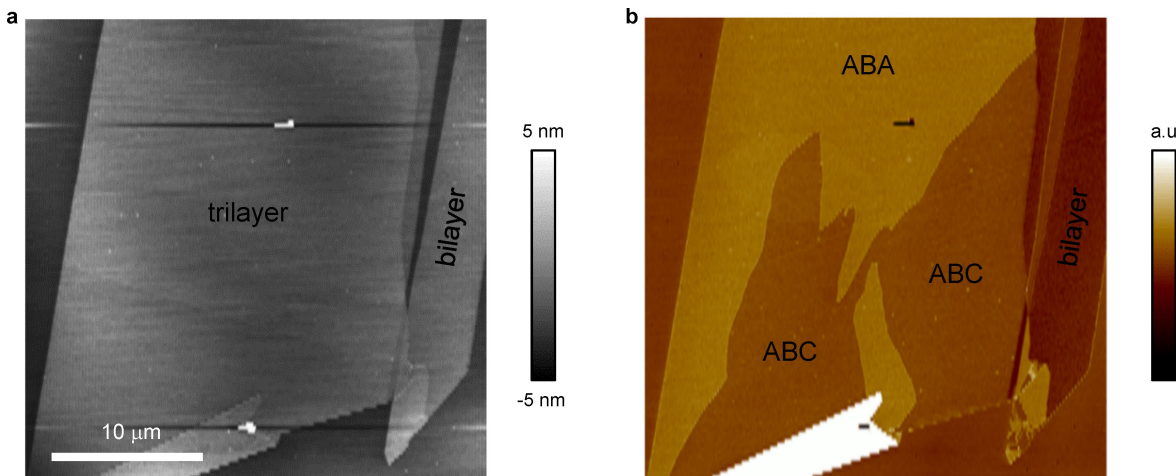
**Competing interests** The authors declare no competing interests.

### Additional information

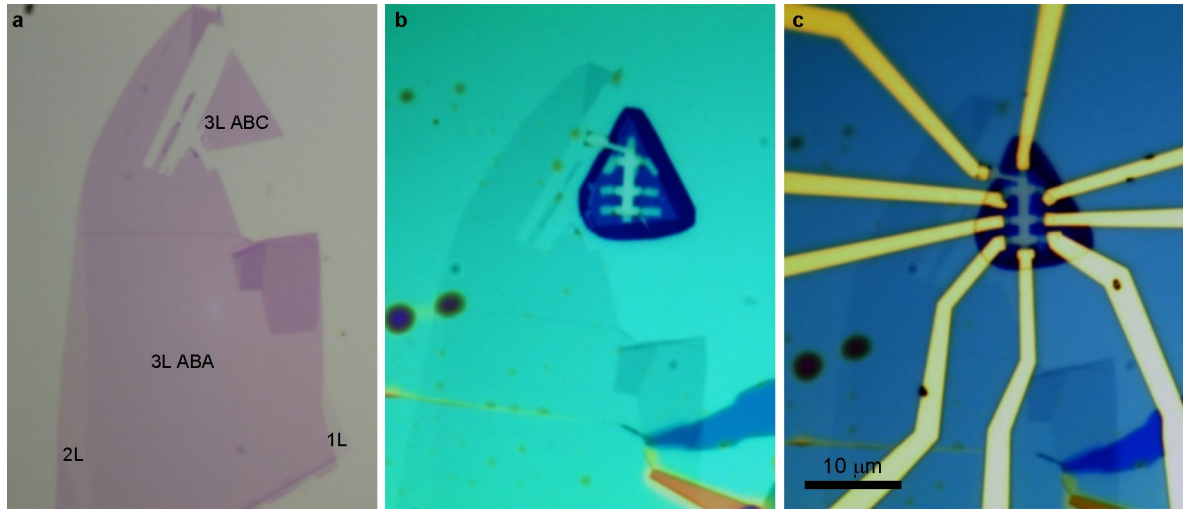
**Correspondence and requests for materials** should be addressed to D.G.-G., Y.Z. or F.W.

**Peer review information** *Nature* thanks Fan Zhang and the other, anonymous, reviewer(s) for their contribution to the peer review of this work.

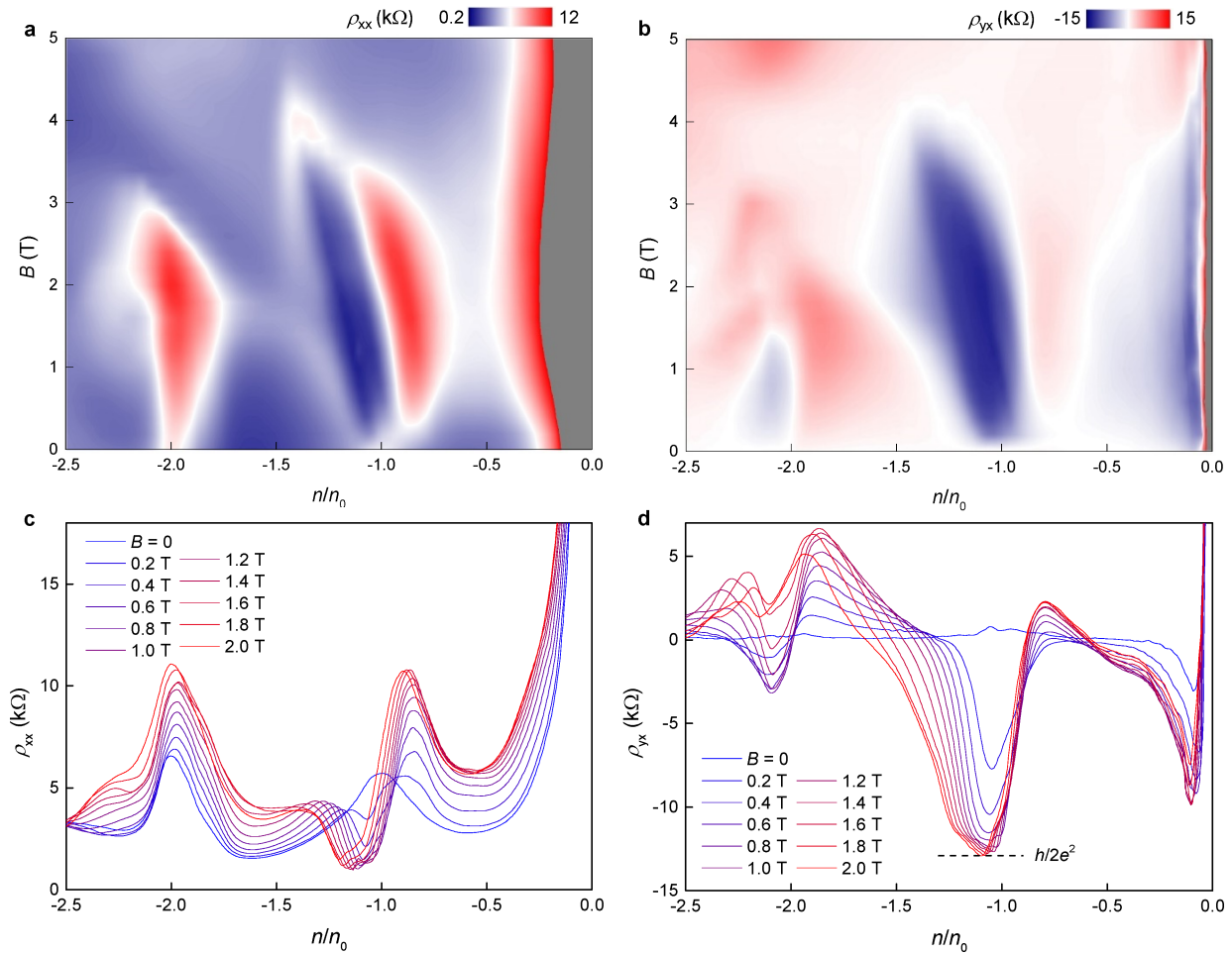
**Reprints and permissions information** is available at <http://www.nature.com/reprints>.



**Extended Data Fig. 1 | Identification of ABC-TLG.** **a**, Atomic force microscope topography image of an exfoliated TLG on  $\text{SiO}_2/\text{Si}$ . **b**, Near-field infrared image corresponding to **a**, showing that ABC-TLG has different contrast to ABA-TLG.

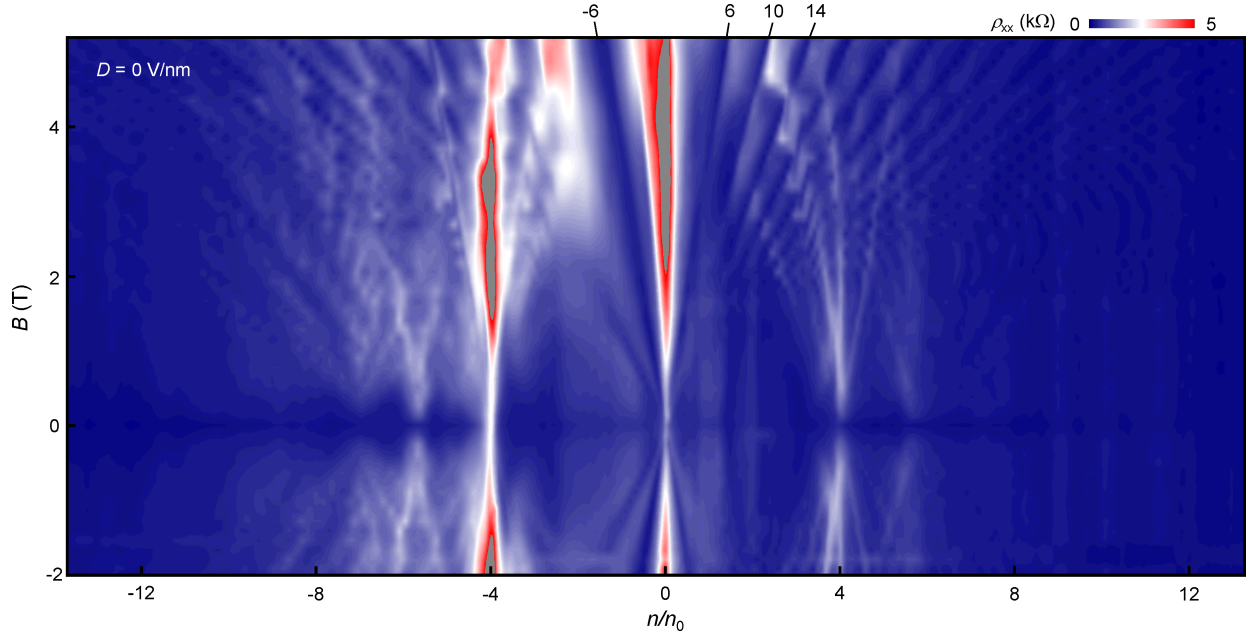


**Extended Data Fig. 2 | Optical images of device I during fabrication.** **a**, ABC-TLG is identified by near-field infrared spectroscopy and isolated by atomic force microscope tip. **b**, ABC-TLG is encapsulated by hBN and etched into Hall bar geometry. **c**, Final device with metal contacts and top and bottom gates.



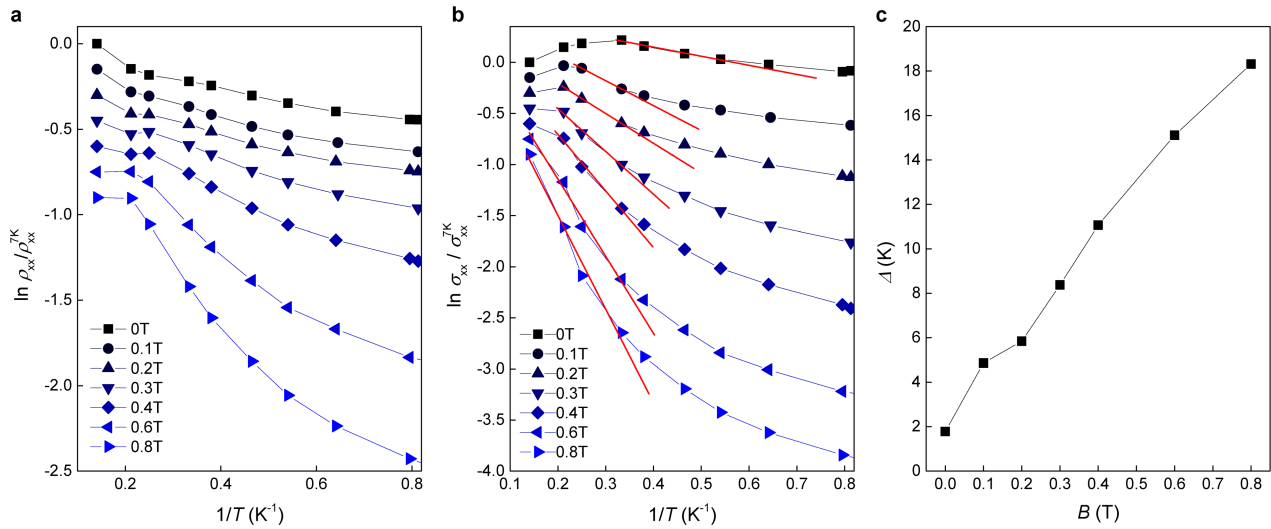
**Extended Data Fig. 3 | Magneto-transport of the Chern insulator state at  $T=1.5\text{ K}$ .** **a, b**, Colour plots of  $\rho_{xx}$  and  $\rho_{yx}$  as a function of carrier density and magnetic field at  $D=-0.5\text{ V nm}^{-1}$  and  $T=1.5\text{ K}$ . The  $v=2$  Chern insulator state is

well resolved at  $1.5\text{ K}$ , which features a minimum for  $\rho_{xx}$ , and a quantized  $\rho_{yx}$  emerges from  $1/4$  filling. **c, d**, Horizontal line cuts of **a** and **b**, respectively.  $\rho_{yx}$  shows quantized Hall resistance at finite magnetic field.



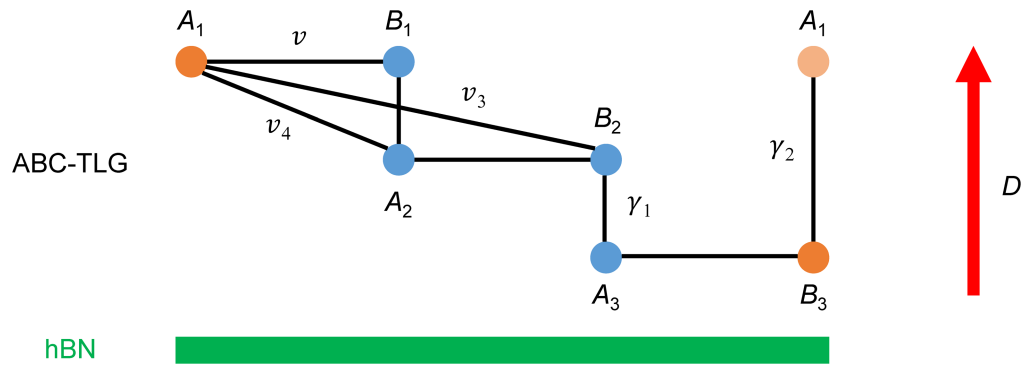
**Extended Data Fig. 4 | Landau fan at  $D=0$ .** Longitudinal resistivity  $\rho_{xx}$  (colour scale) as a function of carrier density and magnetic field at displacement field  $D=0$ . Clear Landau levels develop from the charge neutrality point and fully filled points at  $D=0$ , which is direct evidence of the high quality of the encapsulated ABC-TLG device described in the main text. The first resolved

quantum Hall state of the charge neutrality point is  $v=6$ . This Landau fan diagram establishes conclusively that we have ABC trilayer graphene in the hBN encapsulated device; it is completely different from the Landau fan diagram of ABA trilayer graphene (see ref.<sup>14</sup>).



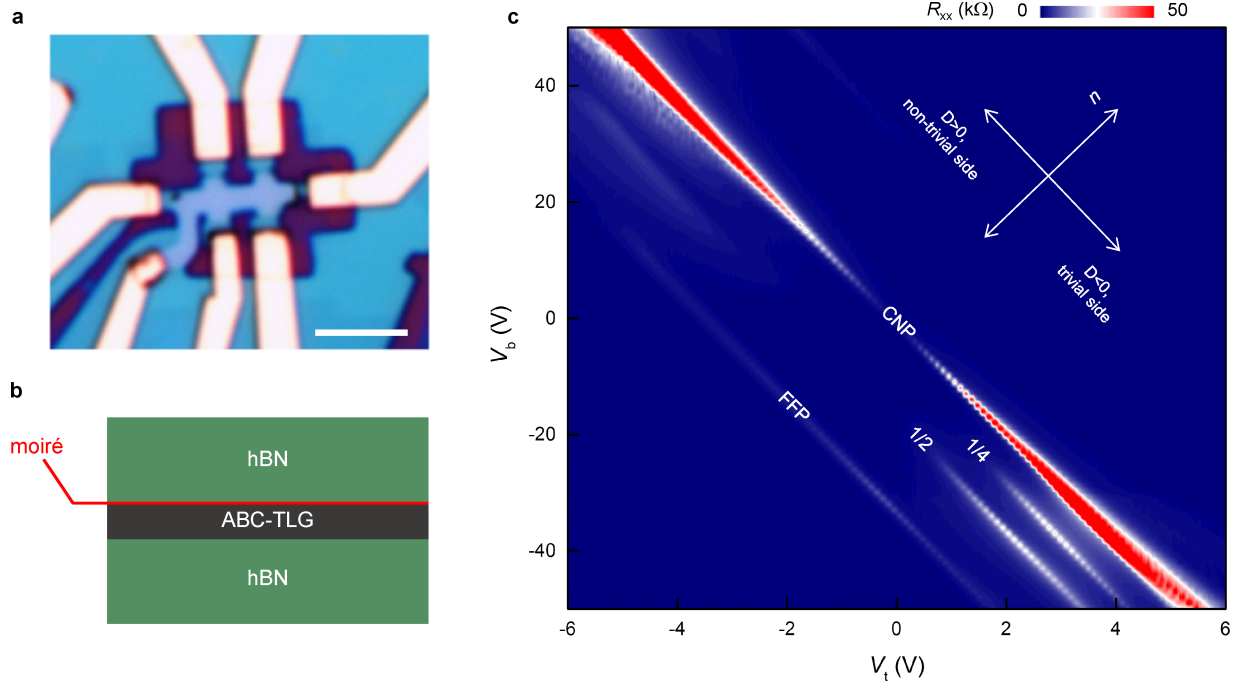
**Extended Data Fig. 5 | Temperature dependence of the  $\nu=2$  state. a–c,** Arrhenius plot of longitudinal resistivity (a), conductivity (b) and the estimated gap at different magnetic field (c). A manual offset of  $-0.15$  on the y axis is applied to each curve in a and b. The gap size in c is extracted from the linear fit of  $\sigma_{xx} \propto e^{-\Delta/2k_B T}$  (red line) in b. We note that the Arrhenius plot is only valid for a limited temperature range, suggesting deviation from the thermal

activated behaviour at low temperatures. Therefore, the estimated gaps have relatively large uncertainty. However, the qualitative behaviour is robust: insulating behaviour is observed at all magnetic fields, and the quantized Hall insulator at finite magnetic field connects smoothly with the anomalous Hall insulator at zero magnetic field, supporting the identification of the state as a Chern insulator.



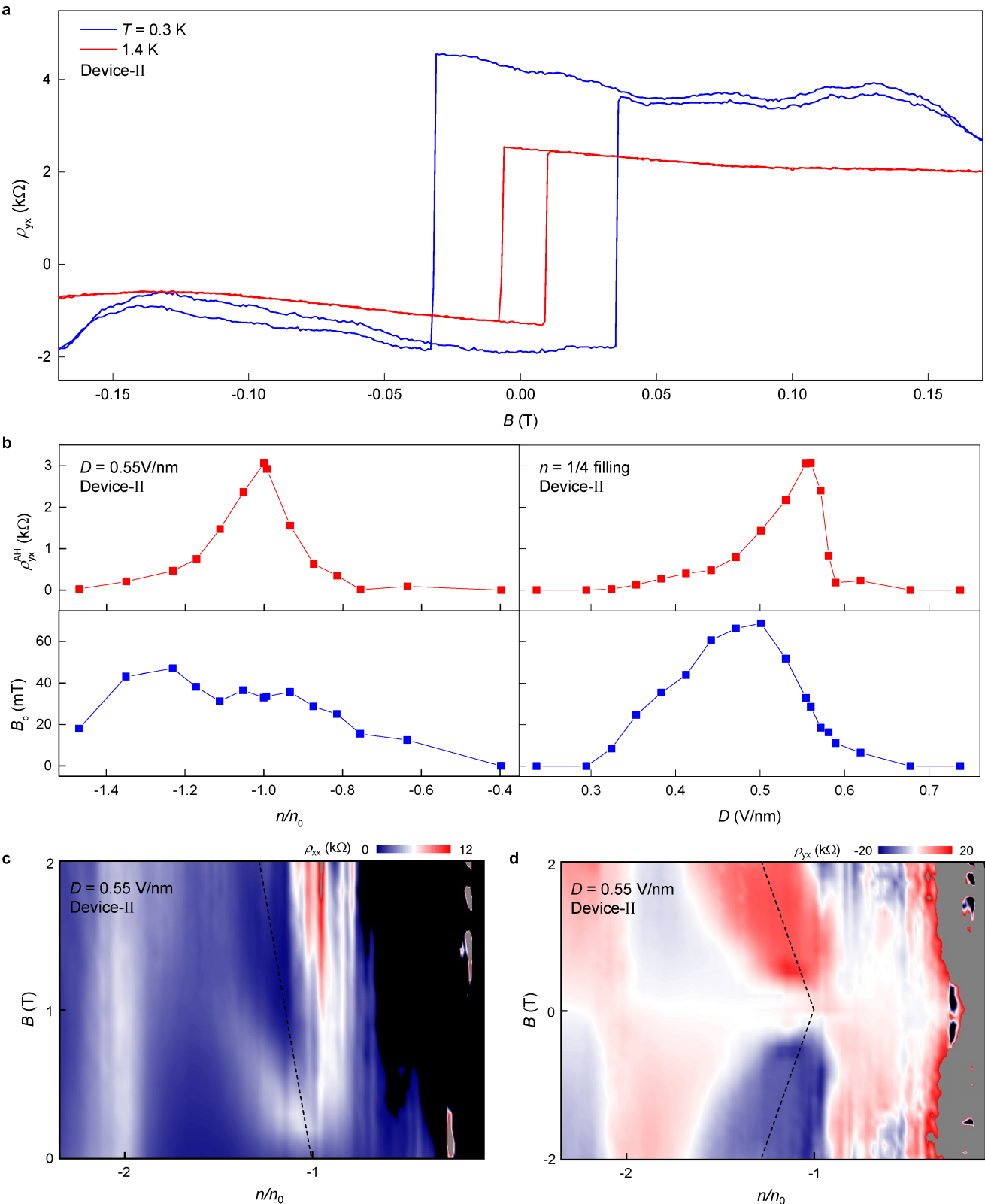
**Extended Data Fig. 6 | Illustration of the ABC-TLG/hBN system.** The bottom hBN layer is nearly aligned with the graphene layers whereas the one on top is not aligned. A and B refer to the two sublattices in each of the graphene layers.

# Article



**Extended Data Fig. 7 | Basic characterizations of the second device (device II).** **a**, Optical image of device II. The device is in a standard Hall bar geometry with top and bottom gates. The scale bar is 3  $\mu\text{m}$ . **b**, Schematic of the moiré pattern existing between top hBN and ABC-TLG for device II. **c**, Two-

dimensional colour plot of  $R_{xx}$  as a function of  $V_t$  and  $V_b$  at  $T=5\text{ K}$ . The moiré exists between the top hBN and ABC-TLG for device II, opposite to that of device I in the main text. This leads to a non-trivial band at positive displacement fields and a trivial band at negative displacement fields.



**Extended Data Fig. 8 | Reproducible Chern insulator data for device II.** **a**, Ferromagnetic anomalous Hall effect at 1/4 filling at 0.3 K and 1.4 K. **b**, The evolution of  $\rho_{yx}^{AH}$  and  $B_c$  as a function of doping (at  $D = 0.55 \text{ V nm}^{-1}$ ) and

displacement field (at  $n = n_0$ ) at 1.1 K. **c, d**, Colour plot of  $\rho_{xx}$  and  $\rho_{yx}$  as a function of carrier density and magnetic field. Dashed lines represent the  $v = 2$  state.